

**Effects of Al on the Creep Behavior and Microstructures in a
(Ni,Fe)Al Precipitate-Strengthened Ferritic Superalloy**

Shenyan Huang

Ph.D. Candidate

Dept. of Materials Science and Engineering, University of Tennessee, Knoxville

TMS Best Paper Contest:

Graduate Division in Physical and Mechanical Metallurgy

Dept. of Materials Science and Engineering

434 Dougherty Hall

The University of Tennessee

Knoxville, TN 37996-2200

Phone: 865-323-0722

Fax: 865-974-4115

Email: shuang4@utk.edu

Effects of Al on the Creep Behavior and Microstructures in a (Ni,Fe)Al Precipitate-Strengthened Ferritic Superalloy

Abstract:

Creep behaviors of (Ni,Fe)Al-strengthened ferritic superalloys as a function of Al compositions were studied for possible steam-turbine applications. A ultra-small-angle X-ray scattering (USAXS) technique was employed to quantify the nanoscale NiAl B2-type precipitates in the aged and crept alloys, with a theoretical model that incorporates polydispersity and interference effects. Complementary transmission-electron-microscopy (TEM) characterizations were performed to compare the microstructural information interpreted from USAXS analysis and to determine the dislocation-particle interaction modes during creep. The effects of Al on the creep behavior and microstructures were discussed in terms of the volume fraction of precipitates and Al concentration in the Fe matrix.

1. Introduction

In order to improve the thermal efficiency of fossil-energy power plants and reduce the emission of CO₂, ultra-supercritical steam (USC) turbines require the steam temperature and pressure to be increased to ultimately 1,033 K and 35 Mpa, respectively [1]. However, current high Cr ferritic steels must be used below 894 K due to their limited creep strength, poor coarsening and steam-corrosion resistance at higher temperatures. Analogue to Ni-based superalloy, the Fe-based β/β' superalloys strengthened by coherent-coplanar ordered (Ni,Fe)Al B2-type (β') precipitates have been designed for USC turbine applications. Their merits include low cost, high thermal conductivity, and low thermal expansion. The microstructure and mechanical properties of NiAl-strengthened Fe-Ni-Al and Fe-Ni-Al-Cr alloys have been studied previously [4-9]. Based on their results, alloy design in the present work has considered the addition of Mo for solid-solution strengthening, B for grain boundary strengthening, and Zr for possible slow diffuser in the matrix, to further improve the creep resistance [2-3]. To obtain a fundamental understanding of the composition-microstructure-property relationships, quantitative analyses of precipitation configurations are required, since the creep behavior is largely dependent on the precipitate parameters through various dislocation-particle interactions (e.g., particle shearing, Orowan bowing, dislocation climb, and dislocation detachment) [10].

In the present work, the creep properties of the six designed ferritic alloys with various amount of Al have been prescreened by compressive-creep experiments. Precipitate parameters have been quantitatively determined, using ex-situ ultra-small-angle X-ray scattering (USAXS) measurements coupled with a theoretical model combining the polydispersity and interference of the precipitates. Complementary TEM characterizations have been carried out to demonstrate the interpretation from the USAXS model and reveal the dislocation-particle interaction mechanisms

in the crept alloys. Effects of Al on the creep behavior and microstructures have been discussed with respect to volume fraction of precipitates and Al composition in the matrix.

Synchrotron USAXS is selected to quantify the precipitates due to its unique advantages over small-angle X-ray scattering (SAXS), small-angle neutron scattering (SANS), laboratory X-ray facilities and transmission-electron microscopy (TEM). It can resolve large-dimension microstructures, including the 130 nm precipitates in the studied alloys, which is below the low-q limit of other small-angle scattering facilities. It probes a large detected volume with better statistics, utilizes a high energy X-ray beam to analyze highly absorbing materials (such as the studied Fe-based superalloys), and requires a short measuring time and small quantity of samples.

2. Experiment

The nominal compositions are listed in Table 1 in weight percent. The alloys were fabricated by vacuum arc-melting, homogenized at 1,473 K for 30 minutes, followed by aging at 973 K for 100 hours. The heat treatments were performed in vacuum, followed by air cooling. Specimens are cut from the ingot into cylinders with a 4-mm diameter and 6-mm height using electrical discharge machining (EDM). Short-time compressive creep tests were conducted to prescreen the creep property of different compositions, using the Material Testing Systems (MTS) facility. A constant compressive load with an initial engineering stress level of 140 MPa was applied at 973 K for 100 hours. After the creep test, the sample was cooled in air. Foils were sliced perpendicular to the cylinder axis for both aged and crept samples and, subsequently, grounded to a thickness of ~ 50 μm . Fine polishing was performed to reduce the contribution from surface scattering. Small-angle scattering data were collected on the X-ray Operations and Research beamline 32-ID-B Ultra-Small-Angle X-ray Scattering Facility [12] at the Advanced Photon Source, Argonne

National Laboratory. Beam energy was tuned to 16.85 keV to ensure roughly 40% transmission from the foils with a beam size of 1.6×0.8 mm. The data reduction and de-smearing were completed to derive the spectra on the absolute intensity scale with Indra and Irena macros [13]. TEM characterization has been carried out in a Hitachi 8100 microscope for aged materials and a FEI Tecnai 20 microscope for crept materials, both operating at 200 kV. For aged samples, slices were cut using a Struers Accutom-5, ground to less than 100 μm in thickness, and thinned by a Fischione dual jet polisher. An electrolyte containing 20% perchloric acid in methanol was maintained at - 35 to - 40°C, and applied by a voltage of 40 V and current of 40 ~ 50 mA. For crept materials, foils used for USAXS measurements were further prepared by electro polishing.

3. Results

3.1 Interpretation of USAXS Data by Theoretical Model

A typical absolute intensity profile from USAXS measurements for the aged FBB6.5 alloy is shown in Fig. 1 as a function of the scattering vector, Q , which contains a power-law slope at $Q < 10^{-3} \text{ \AA}^{-1}$ and a large peak with a small bump at the range of $10^{-3} \sim 10^{-2} \text{ \AA}^{-1}$. The slope at small Q represents the scattering from defects or precipitates at the grain boundaries of the polycrystalline Fe matrix. The large correlation peak is characteristic of the strong interference among precipitates with a non-dilute number density. With the presence of such an interference peak, the Guinier approximation cannot be applied reliably to obtain the radius of gyration as a measure of precipitate size [15]. The position of the peak generally provides the magnitude of the average inter-particle spacing. The smoothness of the measured spectra, for example, the smeared bump at about $7 \times 10^{-3} \text{ \AA}^{-1}$, renders the polydispersity of precipitates and the variance of the inter-particle spacing. All the other intensity spectra for aged and crept alloys with various compositions show

similar characteristic features, except that the position of the correlation peak and its shape varies [see Figs. 3 and 4].

The precipitate parameters in real space can be extracted from the measured absolute intensity in a reciprocal space using theoretical-model fitting. Considering the non-dilute precipitates, we apply a model, including the polydispersity and interference. Previous TEM work showed that B2 precipitates for all the compositions have the spherical shape probably due to the addition of Mo [2,3,9] [see Fig. 1(b)]. For spherical particles, the measured absolute intensity can be written as the product of form and structure factors with other scaling parameters as

$$I(Q) = n_p |\Delta\rho|^2 P(Q)S(Q) + AQ^{-b} + I_{INC} \quad (1)$$

where n_p is the number density of precipitates in the illuminated volume, $\Delta\rho$ is the contrast of the average scattering-length density between the precipitate and the matrix. At small Q , the contribution from the scattering of grain boundaries is taken into account by incorporating a term of AQ^{-b} into the equation, where b is a parameter representing the fractal information of the grain-boundary surface, and A is the scattering amplitude for the grain-boundary scattering. I_{INC} is the incoherent scattering intensity as a background, and $P(Q)$ is the average form factor by shape and size distribution of particles. The normalized form factor for a spherical particle is given by [15]

$$F(Q, x) = [\sin(Qx) - Qx \cos(Qx)] / (Qx)^3 \quad (2)$$

where x is the individual precipitate radius. Considering that precipitates have polydisperse sizes, a normal distribution (Gaussian law) is assumed with an average particle radius, R , and standard deviation of particle radius, δ , as

$$N(x, R, \delta) = \exp\left[-(x - R)^2 / 2\delta^2\right] / \sqrt{2\pi\delta^2} \quad (3)$$

Therefore, the overall expression for the contribution from a form factor is written as

$$P(Q) = \left(\frac{4\pi}{3}\right)^2 \int F^2(Q, x) \cdot N(x, R, \delta) \cdot x^6 dx \quad (4)$$

$S(Q)$, the structure factor representing the inter-particle correlations, is calculated by a stochastic phenomenological model [16]

$$S(Q, L, \sigma) = 2 \left\{ \frac{1 - \exp[-(Q^2 \sigma^2)/4] \cos(QL)}{1 - 2 \exp[-(Q^2 \sigma^2)/4] \cos(QL) + \exp[-(Q^2 \sigma^2)/2]} \right\} - 1 \quad (5)$$

where L is the average inter-particle spacing, and σ is the standard variation of L . Eq. (5) came from the assumption that the particles are partially ordered with an average separation [16]. Such a structure factor has been applied to a Ni-based superalloy system strengthened by ellipsoid precipitates and provided favorable predictions on precipitate parameters [14]. With Eqs. (1) – (5), the measured absolute intensity can be fitted by this model with eight parameters: $n_p |\Delta\rho|^2$, R , δ , L , σ , I_{INC} , b , and A , employing a nonlinear least-squares fitting method.

As exhibited in Fig. 1(a), the agreement between the fitted data and desmeared spectra from the USAXS measurement is excellent. Table 2 lists the fitted average precipitate diameter, average inter-particle spacing, and their corresponding standard deviation from the theoretical model and parameters directly measured by TEM. The fitted precipitate parameters are consistent with the TEM results, while the magnitude of the fitted inter-particle spacing is slightly lower than the values obtained from TEM. The inter-particle spacing by TEM was estimated by the projected distance between particles on the micrograph, and overlapped particles were avoided, which may lead to somewhat overestimation. Overall, the agreement between fitted and measured results for all the aged and crept alloys suggests that the theoretical model provides relatively accurate predictions on the precipitation information.

3.2 Compressive Creep

Figure 2 shows the typical creep curves of strain vs. time for the six alloys. The primary creep stage, where the strain rate decreases as a function of time, is very transient in all the alloys except FBB4, before the material steps into the secondary-creep stage where the strain rate is approximately constant. Either secondary or tertiary creep was achieved during the 100-hours tests. The regime of the secondary creep is relatively shorter in alloys FBB10 and 8 than the other alloys, indicating that microstructure instabilities (e.g., coarsening of precipitates and/or change of dislocation structures) occurred during the steady-state creep and accelerated the onset of the tertiary creep. Steady-state creep rates are plotted in Fig. 4 as a function of Al addition. The total variation in the creep rates was nearly two orders of magnitudes ($10^{-9} \sim 10^{-7}$ /s). Optimal compositions with minimal secondary creep rates were exhibited by the alloys with ~ 6.5 Al% (FBB6.5). Stallybrass [5] measured the compressive steady-state creep rates to be in the range of $7.2 \times 10^{-5} \sim 2.8 \times 10^{-6}$ /s at 973 K and 140 MPa for the Fe-Ni-Al-Cr alloys with 9 \sim 37 volume fractions (vol.%) of precipitates. Compared to his results, FBB alloys show 1 \sim 3 orders of magnitude lower creep rates with less than 20 vol.%. Such incredible improvement in creep resistance is probably attributed to the addition of Mo as a solid solution strengthening element in the Fe matrix. The mobility of dislocation is reduced by moving viscously and dragging the solute atmosphere [22]. The minimal creep rates in solid-solution Fe-Mo were reported to be approximately three orders of magnitude lower than that in α -Fe [23].

3.3 USAXS Results on Aged and Crept Alloys

The variation of the precipitate parameters before and after the creep deformation has been examined. After creep deformation, a common feature for all the alloys is found, i.e., the

correlation peak shifts slightly to the small Q region. Representative plots are displayed in Fig. 3 (a) ~ (e) for aged and crept alloys, with correlation peaks magnified at the lower left corner. The fitted average precipitate diameter, average inter-particle spacing, and their corresponding standard deviation are summarized in Table 3. The inter-particle spacing increases during creep for alloys with differing Al%. The average particle size shows either a constant or slight increment. It reveals that precipitates coarsened slightly during the 100-hour creep deformation. The USAXS intensity profiles measured for the crept alloys with various Al are displayed in Fig. 4. These profiles show similar values of power-law slopes at low Q and incoherent background at high Q . With increasing the Al concentration, the correlation peak shifts to the high Q region, indicating that the inter-particle spacing becomes smaller.

The compiled results of the steady-state creep rate and precipitate parameters interpreted from USAXS were plotted as a function of Al% in Fig. 5. TEM results for the precipitate diameters of the aged alloys are also plotted as a reference to compare with values from USAXS fitting for crept alloys. USAXS results on the aged FBB10 are also plotted as a reference due to the lack of data for the crept alloy. A slight decrease of the fitted precipitate diameter and a dramatic decrease of the spacing are found as Al% increases. Meanwhile, the secondary creep rate first decreases and then increases with a transition at 6.5 Al%.

4. Discussion

The Al content affects the mechanical properties of the ferritic superalloys in three distinct ways: (1) it monitors the precipitation, (2) it modifies the composition of the matrix, and (3) it forms Al_2O_3 oxidation layer on the surface. The first two factors will be discussed as follows.

4.1 Volume Fraction and Creep Behavior

The trends of dramatic and slight decrease of precipitate diameter and spacing imply that the volume fraction of precipitates increases with Al increases. The vol.% in FBB10, 6.5, and 4 have been determined to be 17.9%, 17.8%, and 13.5%, respectively, by analytical electron microscopy (AEM) analyses [2]. It can be concluded that the volume fraction increases as Al increases to 6.5% and saturates with further addition of Al.

Figure 6 presents a typical feature of dislocation-particle interactions examined by TEM, which reveals the existence of two types of strengthening mechanisms: dislocation loops bowing out between particles and dislocation climb around particles. Particle shearing was not observed probably due to the coarse size of precipitates. The results are consistent with Zhu's investigation [7]. These two mechanisms both introduce a threshold stress so that the effective creep deformation is initialized if only the applied stress is higher than the threshold stress. Steady-state creep rate of power-law creep (as suggested by [5,7]) can be expressed as

$$\dot{\epsilon} = B \frac{GbD}{kT} \left(\frac{\sigma_a - \sigma_{th}}{G} \right)^n \quad (6)$$

where B is the dimensionless constant, n is the stress exponent, D is the effective diffusivity of controlled element in the matrix, T is the temperature, G is the shear modulus of matrix, b is the Burger's vector in the matrix, σ_a is the applied stress, and σ_{th} is the threshold stress. The experimental values of n and σ_{th} will be reported in another manuscript [24], which is out of the scope of this paper.

The threshold stress could equal the Orowan stress, or a ratio of the Orowan stress for the dislocation climb (e.g., 0.4 ~ 0.7 for the local climb and 0.004 ~ 0.02 for the general climb mechanisms [10,17]). The Orowan stress can be calculated from the following expression [18]:

$$\sigma_{OR} = \frac{0.81Gb}{\pi\lambda_s(1-\nu)^{1/2}} \ln\left(\frac{1.63r}{b}\right) \quad (7)$$

$$\lambda_s = 0.82 \times \left[\left(\frac{\pi}{f}\right)^{1/2} - 2 \right] r \quad (8)$$

where λ_s is the square lattice spacing, r is the particle radius, f is the volume fraction, and ν is the Poissons Ratio. Using 42 GPa as the shear modulus of Fe at 973K, ν of 0.33, b of 0.20269 nm, and r determined by USAXS, we estimate the Orowan stress for FBB10, 6.5, and 4 to be 190, 143, and 105 MPa, respectively. Assuming that the same mechanism (either dislocation local climb or Orowan bowing), with Al ranging from 4% to 6.5%, the increased volume fraction probably leads to higher threshold stress, and thus largely improves the creep resistance according to Eq. (6). However, such correlation is not valid for alloys with Al > 6.5%. FBB10 has similar volume fraction with FBB6.5, but higher steady-state creep rate than FBB6.5. It is possible that predominant mechanism changes from dislocation loop to local climb or from local climb to general climb at Al > 6.5%, leading to reduced values of threshold stress and increased creep rate for FBB10 and 8.

4.2 Al in the matrix and Creep Behavior

The compositions of both matrix and precipitate phases have been determined by AEM analysis [2]. Figure 7 shows the volume fraction and composition in the matrix and precipitate as a function of Al for FBB10, 6.5, and 4. Although they have the same vol.%, the Al concentration in the matrix is much higher (18.6 at.%) in FBB10 than that (8.2 at.%) in FBB6.5, while the Fe concentration is 10.4 at.% lower as balance. The compositions of other elements in the matrix and elements in the precipitate are similar in the two alloys.

The Al concentration dependence on the inter-diffusion coefficient in the Fe-Al solid solutions

at 1073 ~ 1473 K has been reported [19-21]. Al diffuses much faster than Fe atom in the bcc Fe lattice by a factor of 1 to 2 [19-21]. Both the inter-diffusion coefficient and the self-diffusion coefficient of Fe increase, as Al increases [21]. The vacancy formation enthalpy decreases with increasing Al in Fe-Al alloys and is about 1.4 eV for 7 at.% Al and 1.2 eV for 18 at.% Al [25]. According to Eq. (6), the creep rate is controlled by the diffusivity of the slowest species in the matrix, e.g. Fe self-diffusion [5,7]. Therefore, enhanced diffusion kinetics is one of the possible reasons for the accelerated creep rates with Al > 6.5%.

Lattice parameters of FBB10 and 6.5 at 973 K have been measured by neutron diffraction using General Structure Analysis System (GSAS) Rietveld whole pattern fitting as shown in Figure 8. The addition of Al increases lattice parameters of both matrix and precipitate, from 2.9034Å to 2.9125Å in the matrix and from 2.9040Å to 2.9122Å in the precipitate, for FBB6.5 and 10, respectively. Lattice misfit ($\delta = \frac{a_m - a_p}{a_m}$) is 0.010% for FBB10 and -0.020% for FBB6.5. Negative lattice misfit can generate compressive stress on the precipitate and resist the coarsening to some extent. It agrees with the fact that tertiary creep doesn't appear during 100-hour creep in FBB6.5, in contrast to FBB10.

Al provides solid solution hardening in the Fe-Al alloys and yield stress increases linearly with Al content at room temperature [25]. However, Al concentration dependence on yield stress at temperature above 923 K becomes relatively weak [26], which may not affect the creep properties. Other possible effects of concentrated Al in the matrix on the accelerated creep rates, involving the grain boundary structures and minor phases, will be further investigated as future work.

5. Conclusion

- (1) The USAXS is used to measure precipitate parameters in the ferritic superalloy. A theoretical model that incorporates a polydisperse form factor and a phenomenological structure factor is employed to predict the precipitate size, spacing, and corresponding variances. Fitted results compare favorably with the measured spectra and complementary TEM characterizations.
- (2) As the amount of Al increases in the alloys, a dramatic and slight decrease of the average inter-particle spacing and particle diameter were observed, respectively. Optimal compositions with superior creep resistance contain ~ 6.5 Al%. Orowan bowing and dislocation climb are possible dislocation-particle interaction mechanisms.
- (3) Steady-state creep rates declined in the region of 4 ~ 6.5 Al% due to an increased volume fraction of precipitates and enhanced resistance to dislocation motion. Accelerated creep rates were found in the region of 6.5 ~ 10 Al%, associated with high Al concentration in the matrix or change of dislocation-particle interaction mechanism.

Acknowledgement:

This work was supported financially by the US Department of Energy (DOE), Office of Fossil Energy, under Grant No. DE-FG26-06NT42732 and DE-09NT0008089, with program managers Dr. Patricia Rawls and Vito Cedro. Use of the Advanced Photon Source was supported by the U. S. Department of Energy, Office of Science, Office of Basic Energy Sciences, under Contract No. DE-AC02-06CH11357. TEM of the crept alloys were performed at the SHaRE (SHared Research Equipment) User Facility, which is sponsored by the Division of Scientific User Facilities, Office of Basic Energy Sciences, the U.S. Department of Energy.

Reference:

- [1] Bhadeshia HKDH. *ISIF International* 2001;41:626.
- [2] Teng ZK, Liu CT, Ghosh G, Liaw PK, Fine ME. *Intermetallics*, doi:10.1016/j, 2010.
- [3] Teng ZK, Miller MK, Ghosh G, Liu CT, Huang S, Russel KF, Liaw PK. *Scripta Mater.* 2010;63:61.
- [4] Stallybrass C, Sauthoff G. *Materials Science and Engineering A* 2004;387:985.
- [5] Stallybrass C, Schneider A, Sauthoff G. *Intermetallics* 2005;13:1263.
- [6] Taillard R, Pineau A, Thomas BJ. *Materials Science and Engineering* 1982;54:209.
- [7] Zhu SM, Tjong SC, Lai JKL. *Acta Materialia* 1998;46:2969.
- [8] Calderon HA, Fine ME. *Materials Science and Engineering* 1984;63:197.
- [9] Calderon HA, Fine ME, Weertman JR. *Metallurgical Transactions A-Physical Metallurgy and Materials Science* 1988;19:1135.
- [10] Kassner ME. *Fundamentals of creep in metals and alloys*. Elsevier, 2004.
- [11] Kostorz G. X-ray and Neutron Scattering, in *Physical metallurgy*, 4th ed., edited by Cahn RW and Haasen P, pp. 1115-1199. Amsterdam: North-Holland.
- [12] Ilavsky J, Jemian PR, Allen AJ, Zhang F, Levine LE, Long GG. *J. Appl. Crystallogr* 2009;42:469.
- [13] Ilavsky J, Jemian PR. *J. Appl. Crystallogr* 2009;42:347.
- [14] Huang EW, Liaw PK, Porcar L, Liu Y, Liu YL, Kai JJ, Chen WR. *Appl. Phys. Lett.* 2008;93.
- [15] Zemb T, Lindner P, Zemb Th. *Neutron, X-rays and Light. Scattering Methods Applied to Soft Condensed Matter*. Elsevier, 2002.
- [16] Farsaci F, Fontanella ME, Salvato G, Wanderlingh F, Giordano R, Wanderlingh U. *Physics and Chemistry of Liquids* 1989;20:205.
- [17] Brown LM, Ham RK, in: Kelly A, and Nicholson RB (Eds.), *Strengthening Methods in Crystals*, Elsevier, Amsterdam, 1971, p. 75.
- [18] Martin JW, *Micromechanisms in Particle-Hardened Alloys*, Cambridge University Press, Cambridge, U.K., 1980, p. 43.
- [19] Hirano K, Hishinuma A. *Journal of the Japan Institute of Metals* 1968;32:516.
- [20] Nishida K, Yamamoto T, Nagata T. *Transactions of the Japan Institute of Metals* 1971;12:310.
- [21] Sohn YH, Dayananda MA. *Scr. Mater.* 1998;40:79.
- [22] Terada D, Yoshida F, Nakashima H, Abe H, Kadoya Y. *ISIJ Int.* 2002;42:1546.
- [23] Kadoya Y, Shimizu E. *Tetsu To Hagane-J. Iron Steel Inst. Jpn.* 1999;85:827.
- [24] Huang S, Kenik E, Teng ZK, Wang G, Fine ME, Liu CT, Ghosh G, Liaw PK. *Tensile Creep Behavior of NiAl-Strengthened Ferritic Superalloys with Addition of Mo and W. In preparation.*
- [25] Herrmann J, Inden G, Sauthoff G. *Acta Mater.* 2003;51:2847.
- [26] Herrmann J, Inden G, Sauthoff G. *Acta Mater.* 2003;51:3233.

Table 1 FBB alloy nominal compositions (weight percent, wt.%)

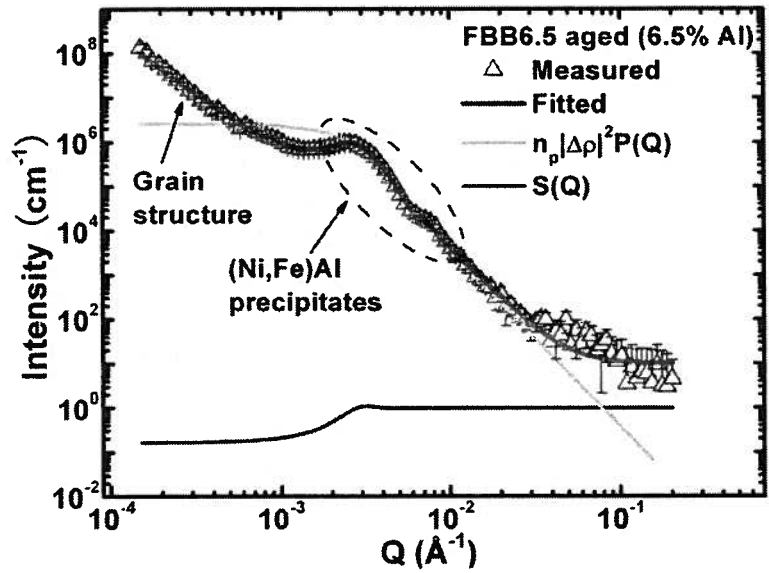
Alloys #	Fe	Al	Cr	Ni	Mo	Zr	B
FBB10	66.3	10	10	10	3.4	0.25	0.005
FBB8	68.3	8	10	10	3.4	0.25	0.005
FBB6.5	69.8	6.5	10	10	3.4	0.25	0.005
FBB6	70.3	6	10	10	3.4	0.25	0.005
FBB5	71.3	5	10	10	3.4	0.25	0.005
FBB4	72.3	4	10	10	3.4	0.25	0.005

Table 2 Precipitate parameters of the aged FBB6.5 alloy determined by fitting to the USAXS measurements and TEM characterizations.

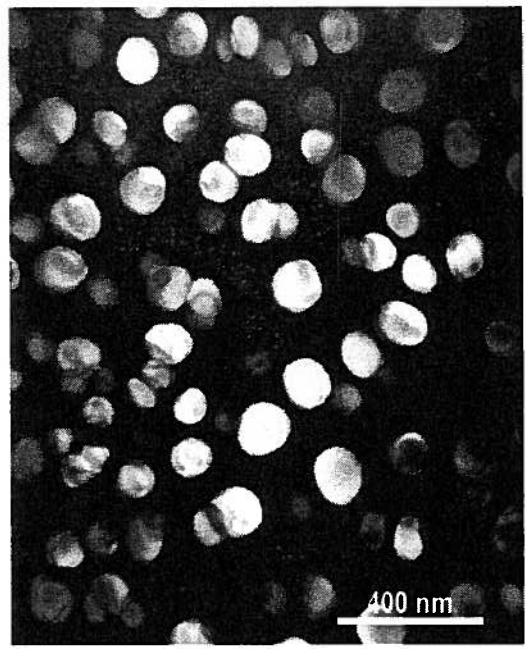
Parameters	USAXS	TEM
Average diameter of precipitates	129.8 nm	130.0 nm
Standard deviation of diameter	30.0 nm	25.0 nm
Average inter-particle spacing	175.0 nm	211.0 nm
Standard deviation of inter-particle spacing	101.7 nm	37.5 nm

Table 3 Precipitate parameters of the aged and crept FBB alloys determined by fitting to the USAXS measurements (units: nm).

Parameters	FBB4		FBB5		FBB6		FBB6.5		FBB8		FBB10
	Aged	Crept	Aged	Crept	Aged	Crept	Aged	Crept	Aged	Crept	Aged
Average diameter	152.4	302.0	127.4	117.4	111.0	119.4	129.8	119.0	99.4	109.4	89.6
Standard deviation of diameter	38.4	32.6	34.8	35.0	32.0	27.8	30.0	29.2	24.4	17.9	22.4
Average spacing	302.0	333.1	229.5	240.4	186.6	183.9	175.0	210.9	178.5	196.9	180.1
Standard deviation of spacing	174.0	176.0	196.5	107.0	89.2	101.6	101.7	84.7	74.2	82.2	78.6



(a)



(b)

Figure 1 (a) Measured and fitted absolute intensity profiles for the aged FBB6.5 alloy, along with scaled form factor and structure factor, and (b) the dark-field (DF) (using 100_{B2} reflection) micrograph of the aged FBB6.5 alloy showing $B2$ (bright) domains.

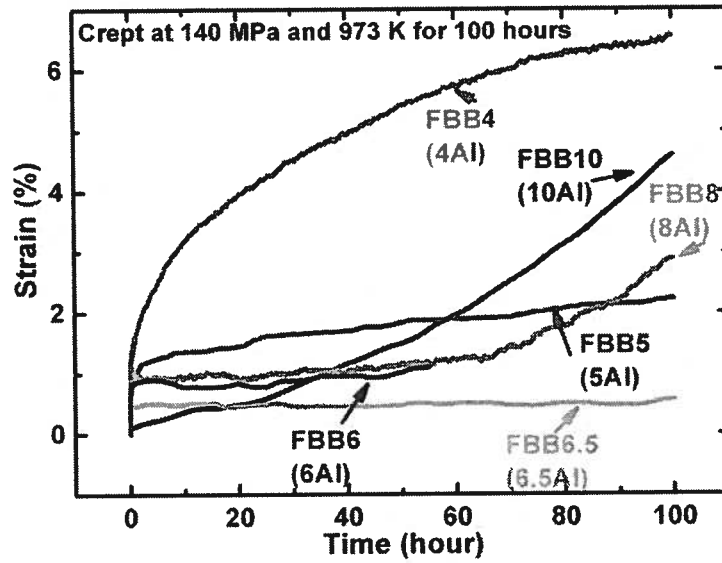


Figure 2 Compressive creep curves for various compositions plotting strain as a function of time.

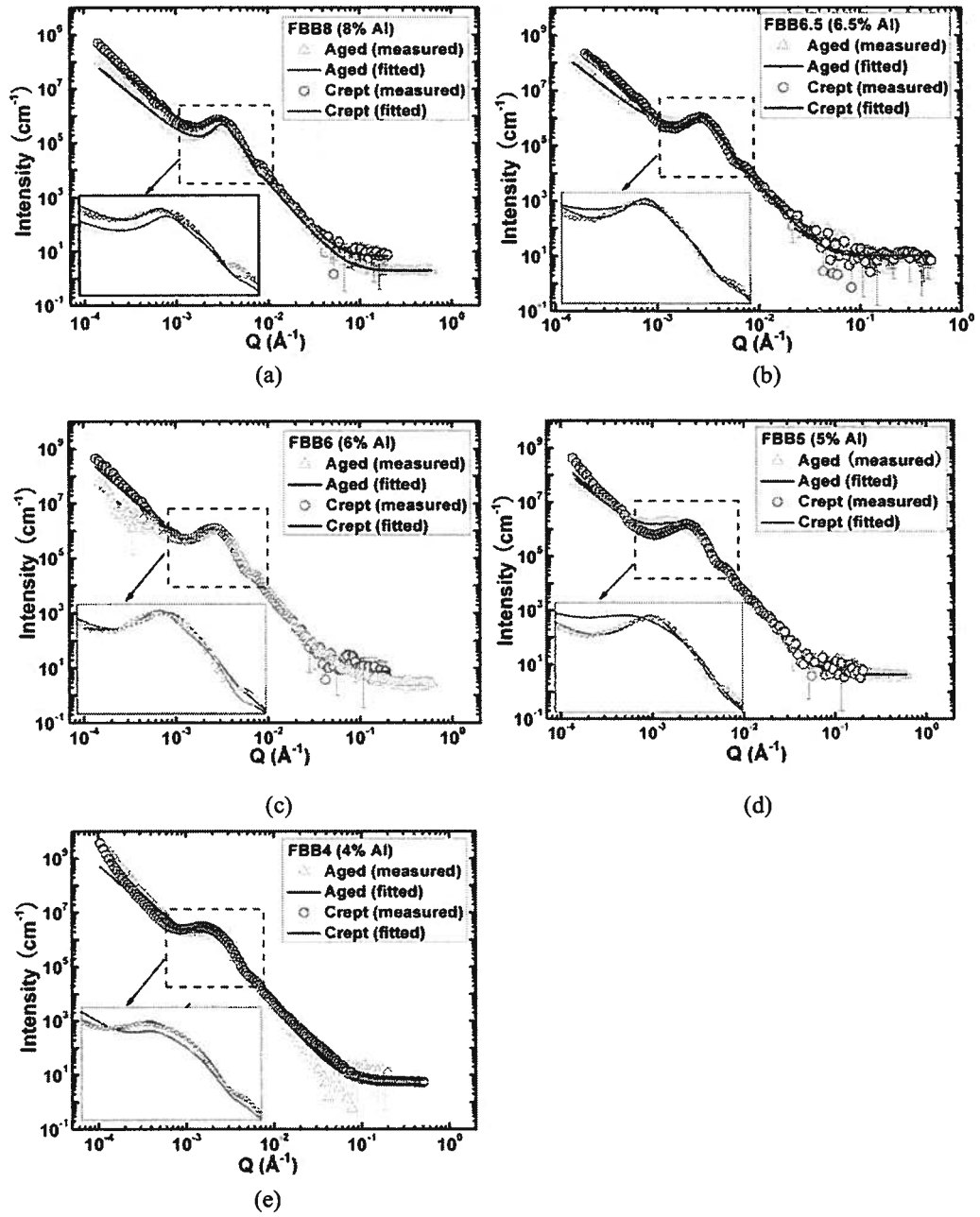


Figure 3 Measured and fitted absolute intensity profiles for aged and crept FBB alloys with 8 ~ 4% Al [(a) ~ (e)].

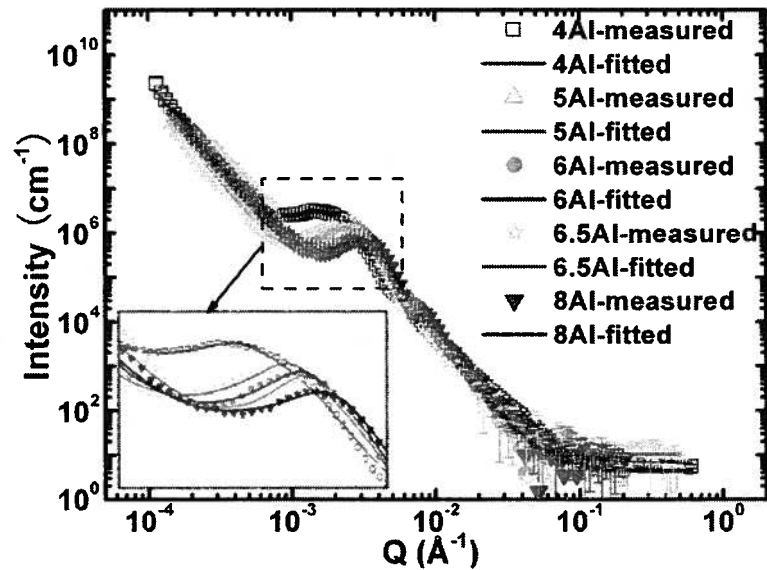


Figure 4 Measured and fitted absolute intensity profiles for crept ferritic alloys with different Al%.

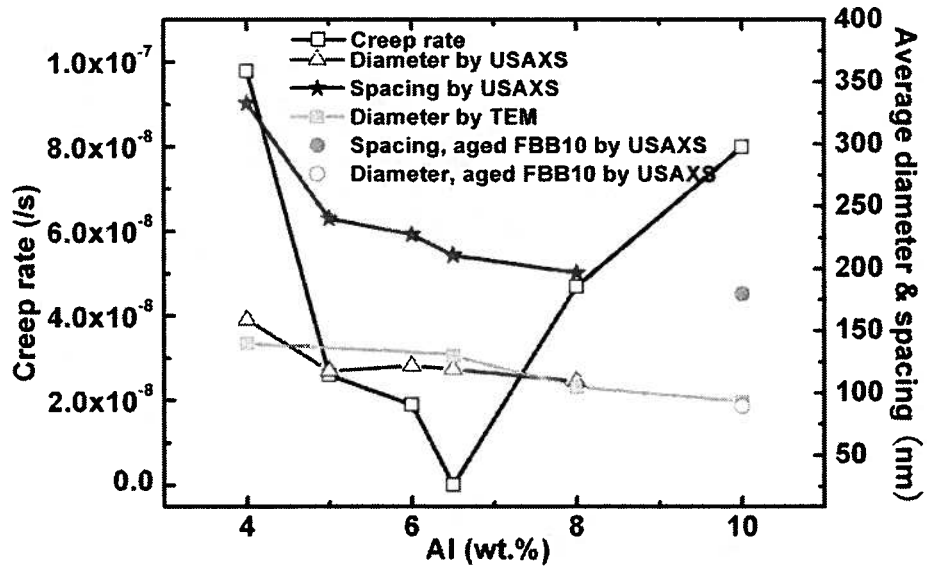
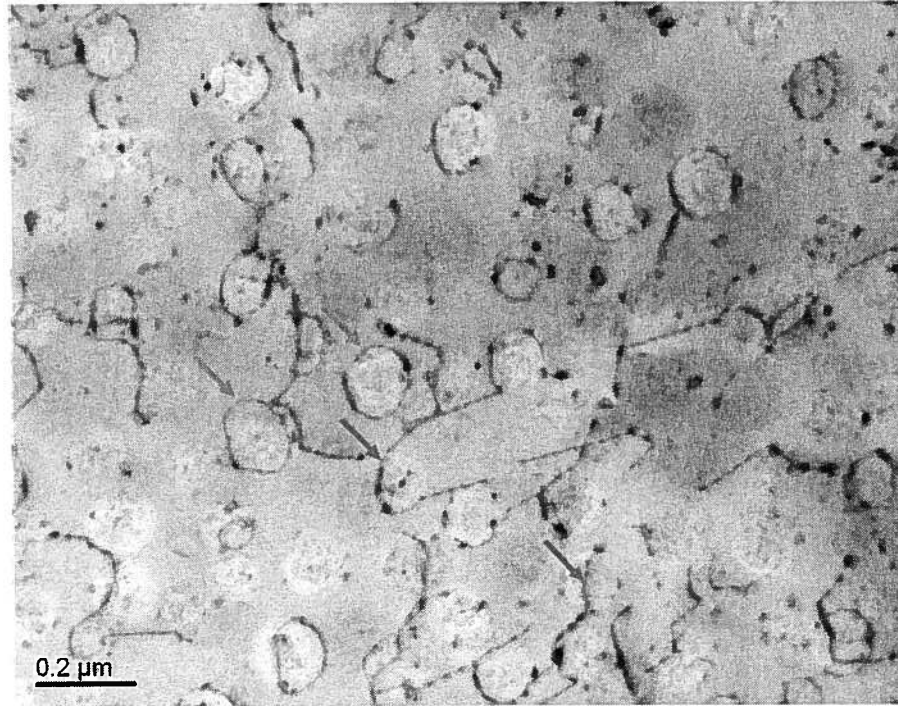
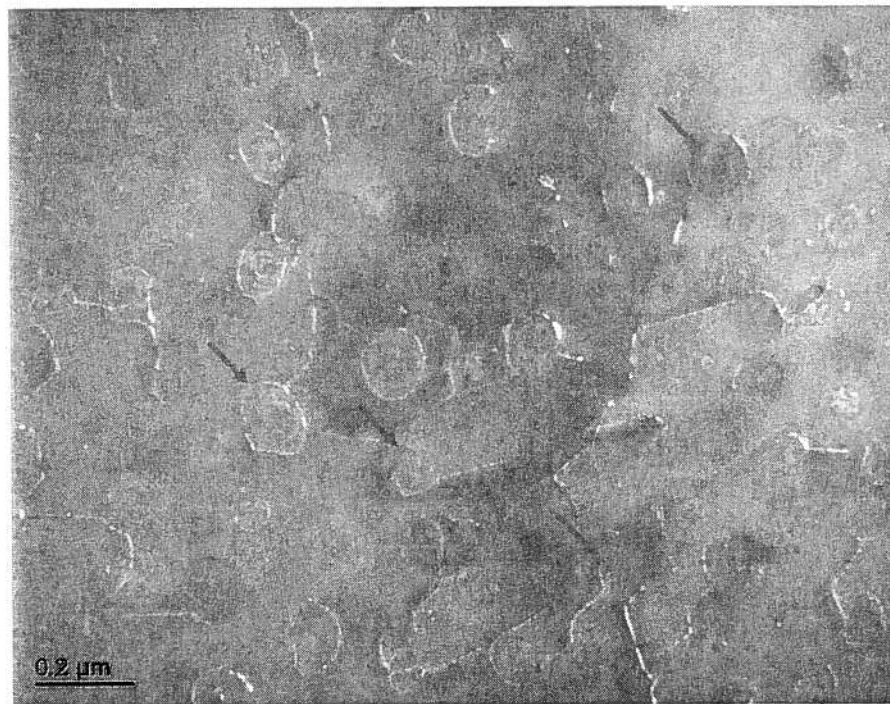


Figure 5 Secondary creep rate, predicted precipitate parameters for the crept specimen, and measured precipitate diameter for aged alloys by TEM as a function of Al%. Spacing and diameter of precipitates for aged FBB10 alloy are denoted by orange closed and open circles, respectively.

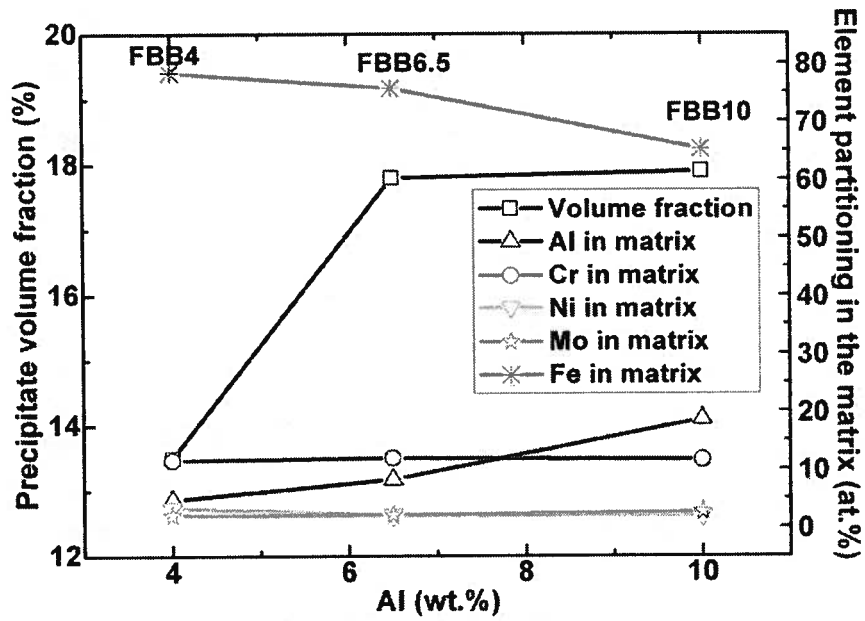


(a)

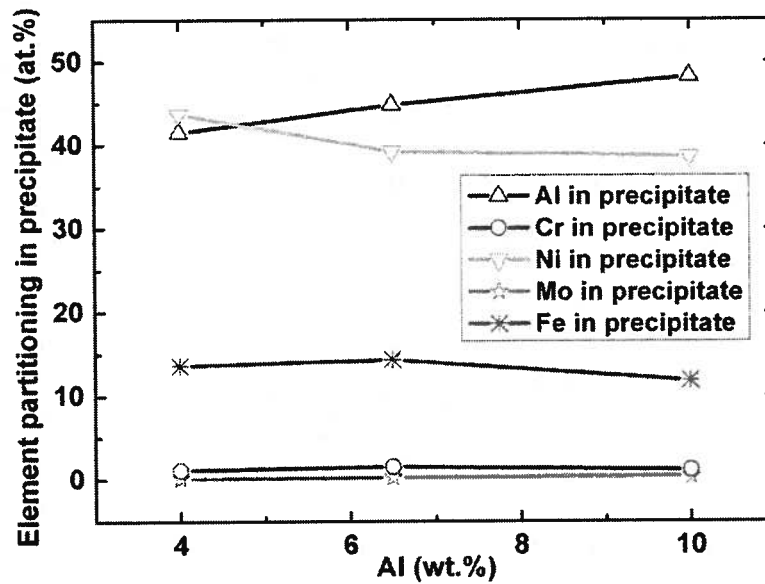


(b)

Figure 6 (a) Bright-field (BF) and (b) dark-field (DF) micrographs of dislocation-particle interactions identified as the Orowan bowing (dislocation loop) (red arrows) and dislocation climb (blue arrows) in the compressively crept FBB8.

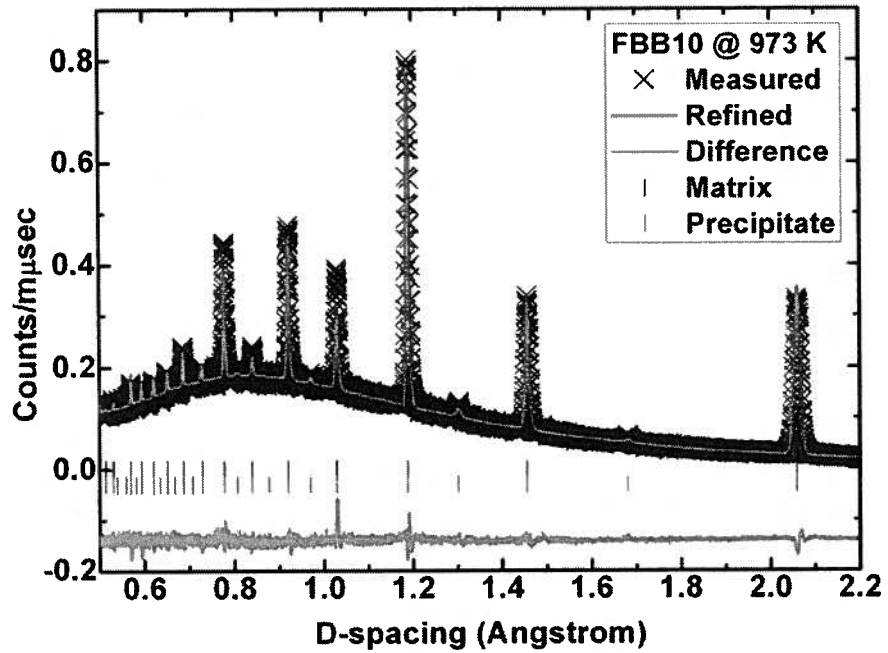


(a)

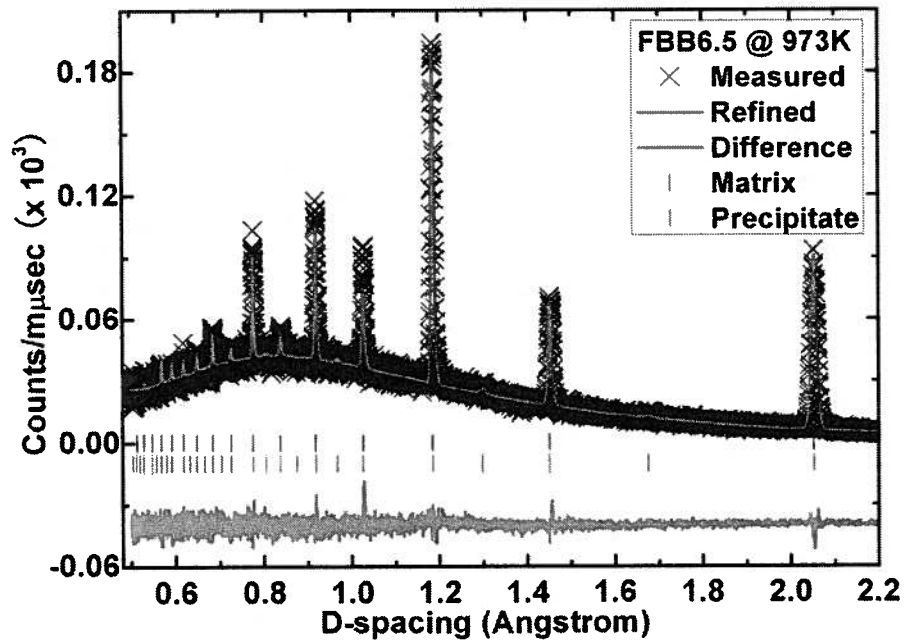


(b)

Figure 7 (a) Volume fraction and element partitioning in the matrix, and (b) element partitioning in the precipitate determined by AEM analysis for FBB10, 6.5, and 4.



(a)



(b)

Figure 8 Neutron diffraction pattern of (a) FBB10 and (b) FBB6.5 at 973 K by GSAS Rietveld whole pattern fitting.